Supplement of Atmos. Chem. Phys., 23, 15011–15038, 2023
https://doi.org/10.5194/acp-23-15011-2023-supplement

Atmospheric Chemistry and Physics
Open Access

Supplement of

Characterizing the near-global cloud vertical structures over land using high-resolution radiosonde measurements

Hui Xu et al.

Correspondence to: Jianping Guo (jpguocams@gmail.com) and Bing Tong (bingtong@rcees.ac.cn)

FIGURES

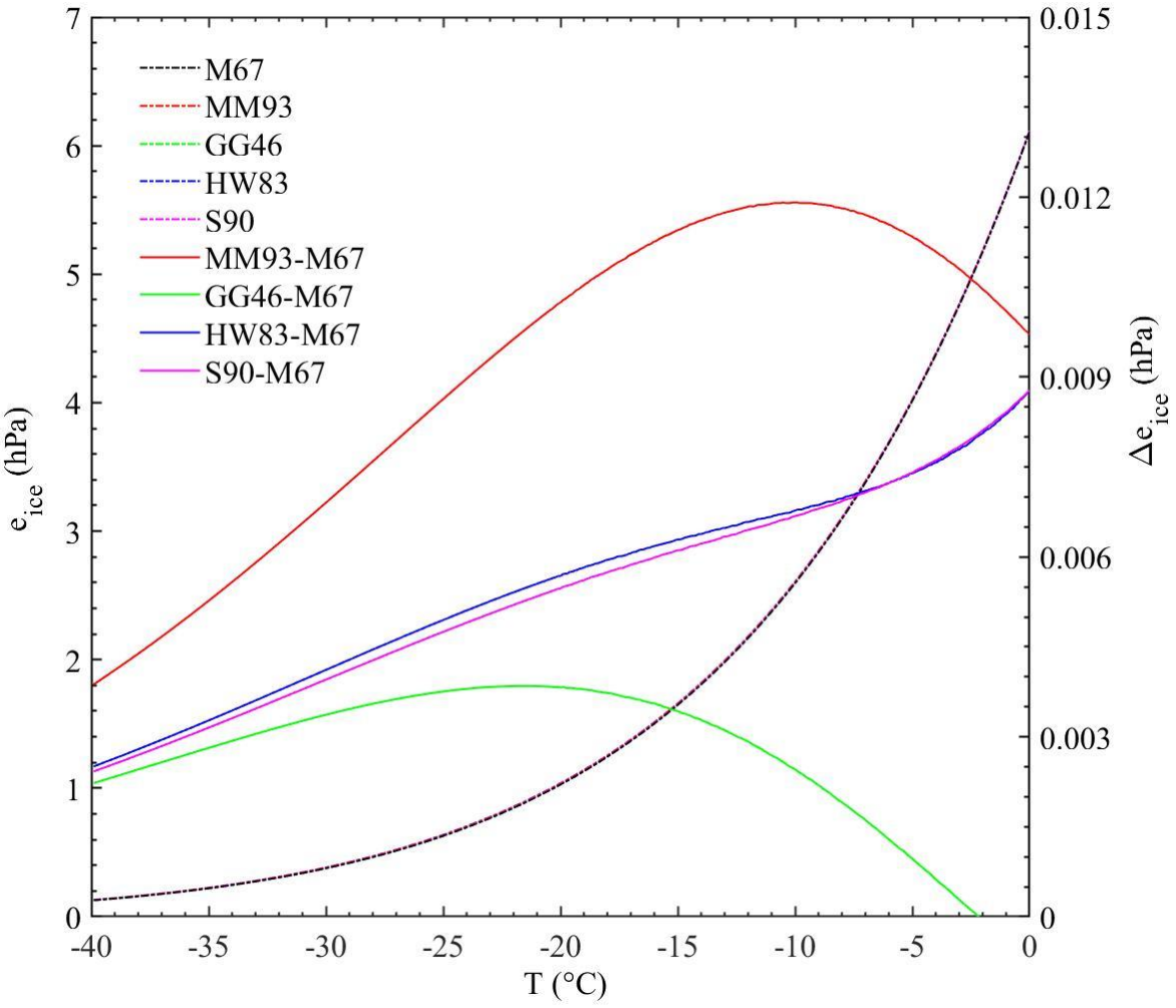

Figure S1. The saturation vapor pressure in the pure ice phase (e_{ice}) for – 40 to 0 °C calculated by the expression in Murray (1967) (M76), Marti and Mauersberger (1993) (MM93), Goff and Gratch (1946) (GG46), Hyland and Wexler (1983) (HW83), and Sonntag (1990) (S90). Also shown is the absolute difference in e_{ice} between M76 with MM93, GG46, HW83, and S90, respectively.

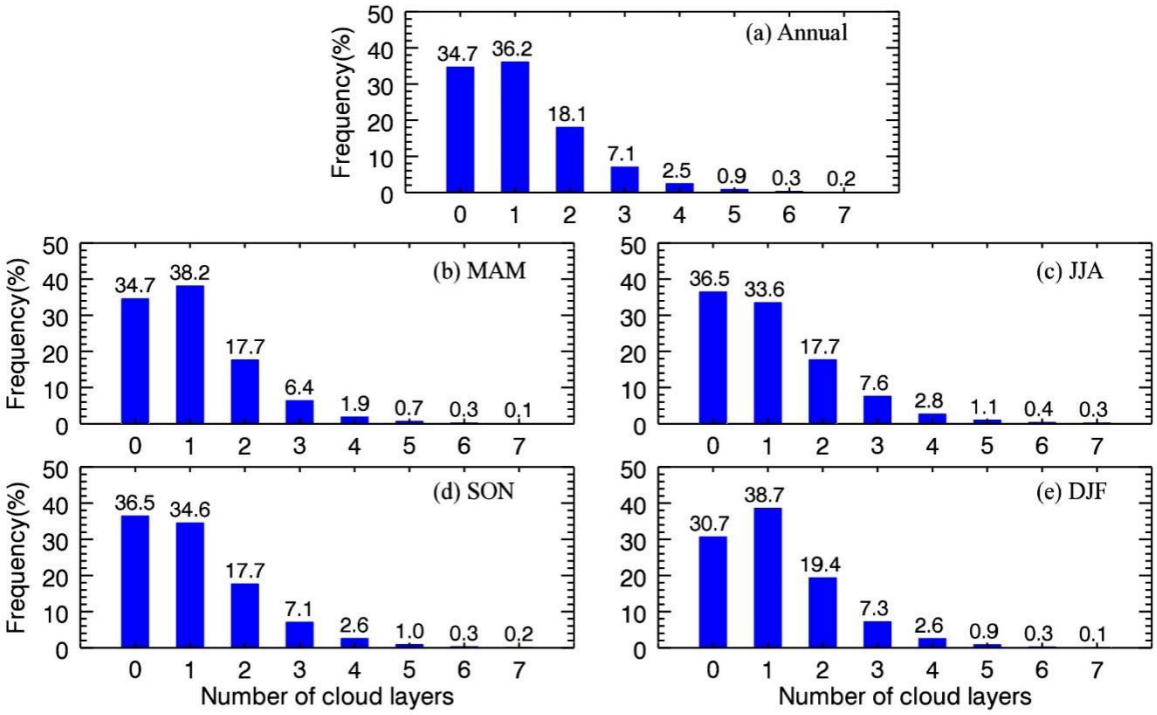

Figure S2. Near-global mean occurrence frequencies of clouds with a variety of layers ranging from 0 to 7 as detected by high-resolution radiosonde measurements at 0000 UTC during the period of 2018–2019: (**a**) annual, (**b**) March–April–May (MAM), (**c**) June–July–August (JJA), (**d**) September–October–November (SON), and (**e**) December–January–February (DJF). Also marked is the probability for the specified cloud type at the top of each bar.

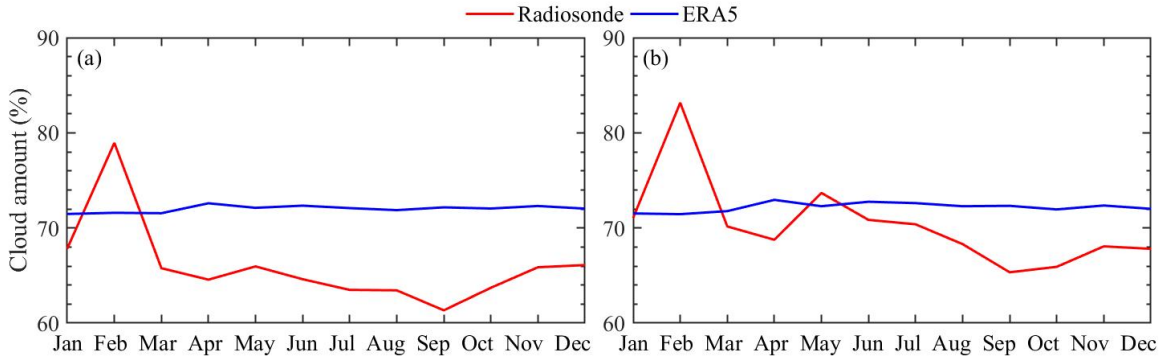

Figure S3. The monthly cloud fraction at (**a**) 0000 UTC, and (**b**) 1200 UTC. The red and blue lines represent the cloud amount from radiosonde and ERA5, respectively.

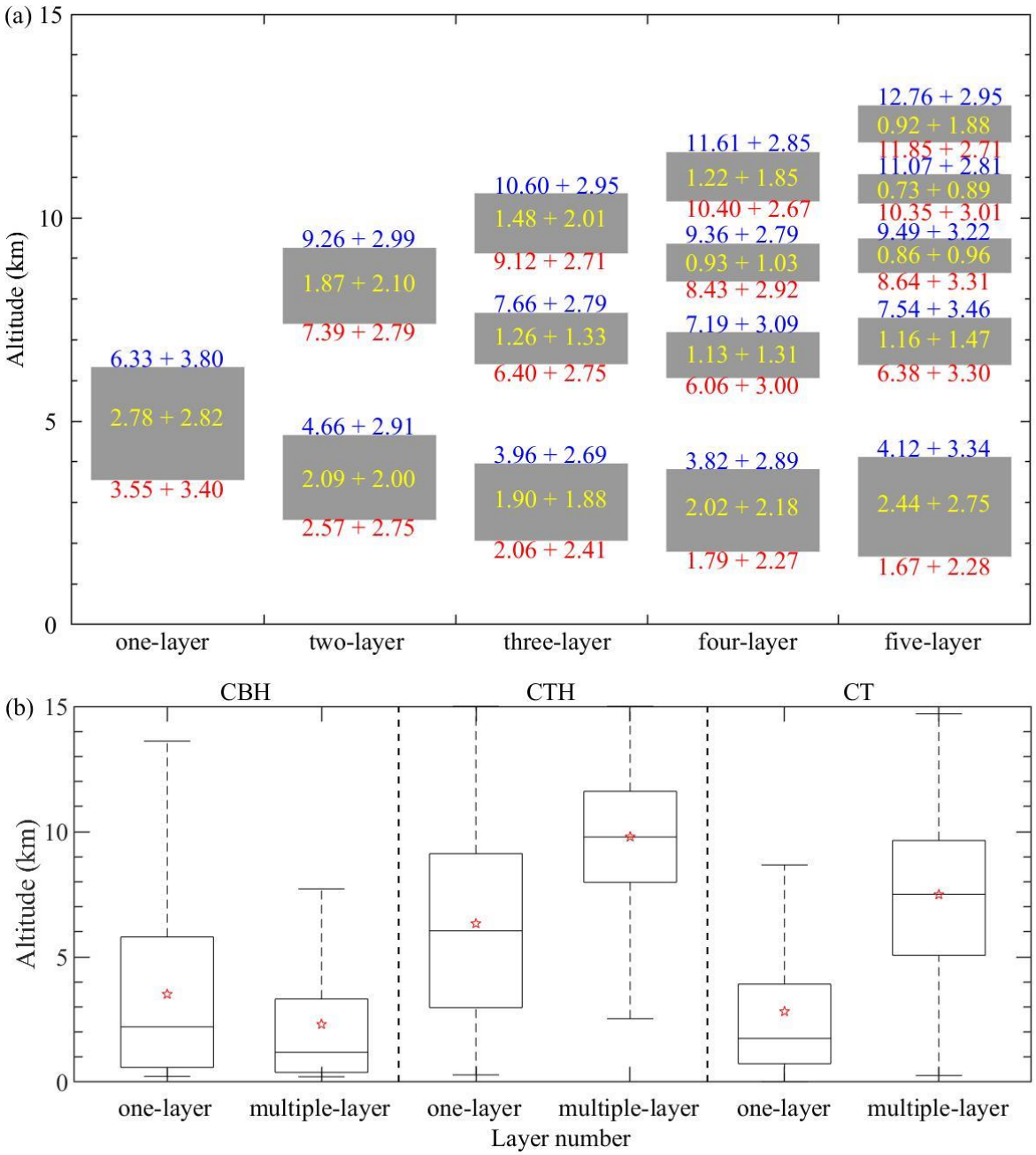

Figure S4. Near-global annual mean (**a**) vertical locations of one-, two-, three-, four-, and five-layer clouds and (**b**) boxplot of CVS (CBH, CTH, and CT) for one- and multi-layer clouds at 0000 UTC during the period of 2018–2019. The mean ± one standard deviation values of CBH, CTH, and CT for each cloud type are also marked in (**a**).

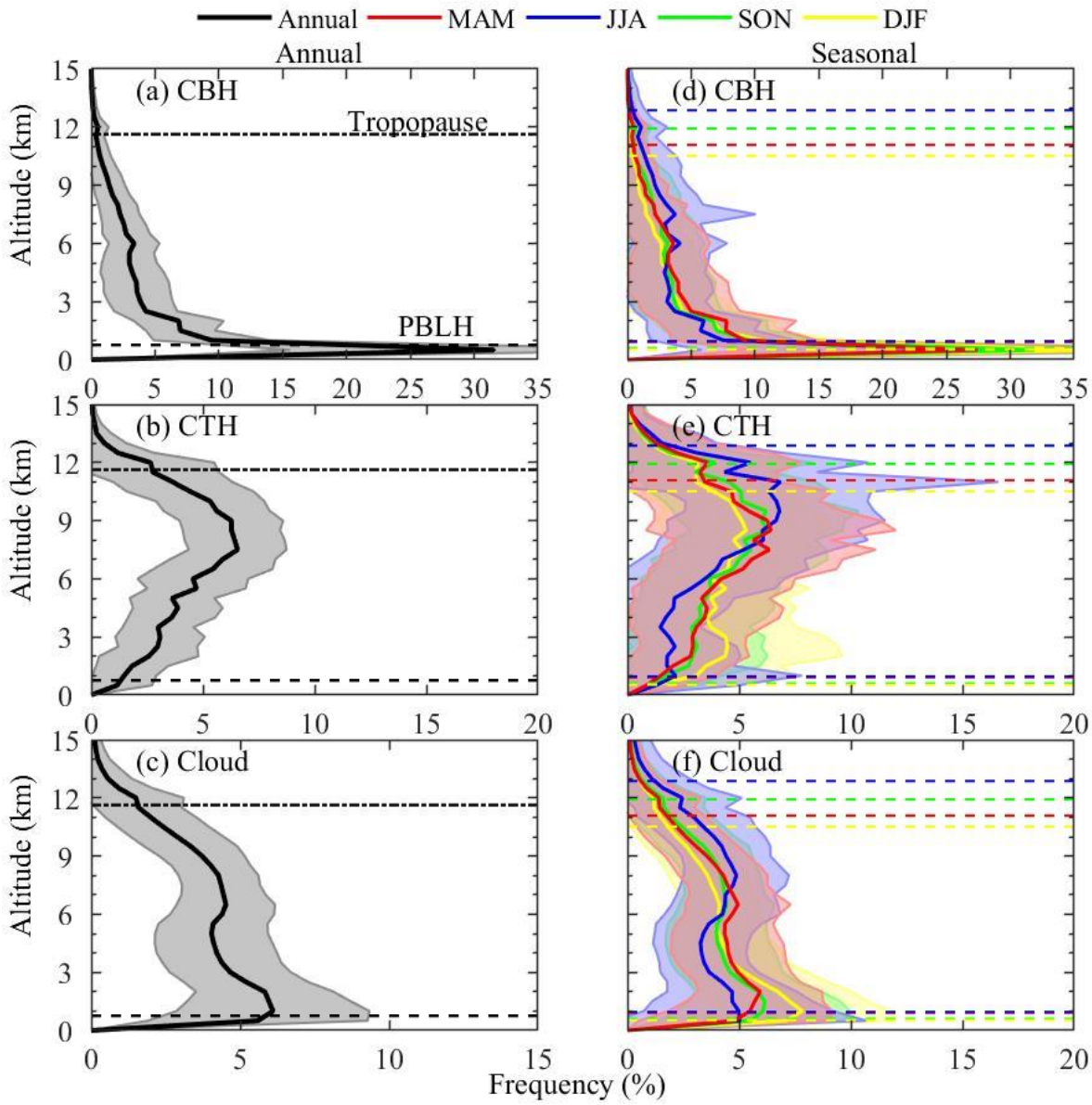

Figure S5. Near-global mean vertical distributions of (**a**, **b**, and **c**) annual and (**d**, **e**, and **f**) seasonal occurrence frequencies of CBHs, CTHs, and clouds as detected by radiosonde data at 0000 UTC during the period of 2018–2019, respectively. The annual, MAM, JJA, SON, and DJF are marked in black, red, blue, green, and yellow, respectively. Samples are vertically divided with a resolution of 500 m. The percentage for a given altitude is defined as the ratio of cloudy samples on that altitude to all cloudy samples. The solid lines are the mean values and shadows are the one standard deviation at annual or a given season. The planetary boundary layer height (PBLH) is determined with the method proposed by Vogelezang and Holtslag (1996), marked in dot-hyphen, and the tropopause is defined with the method from WMO (1957), marked in hyphen. The determination of PBLH and tropopause are detailed in the Supplementary Information.

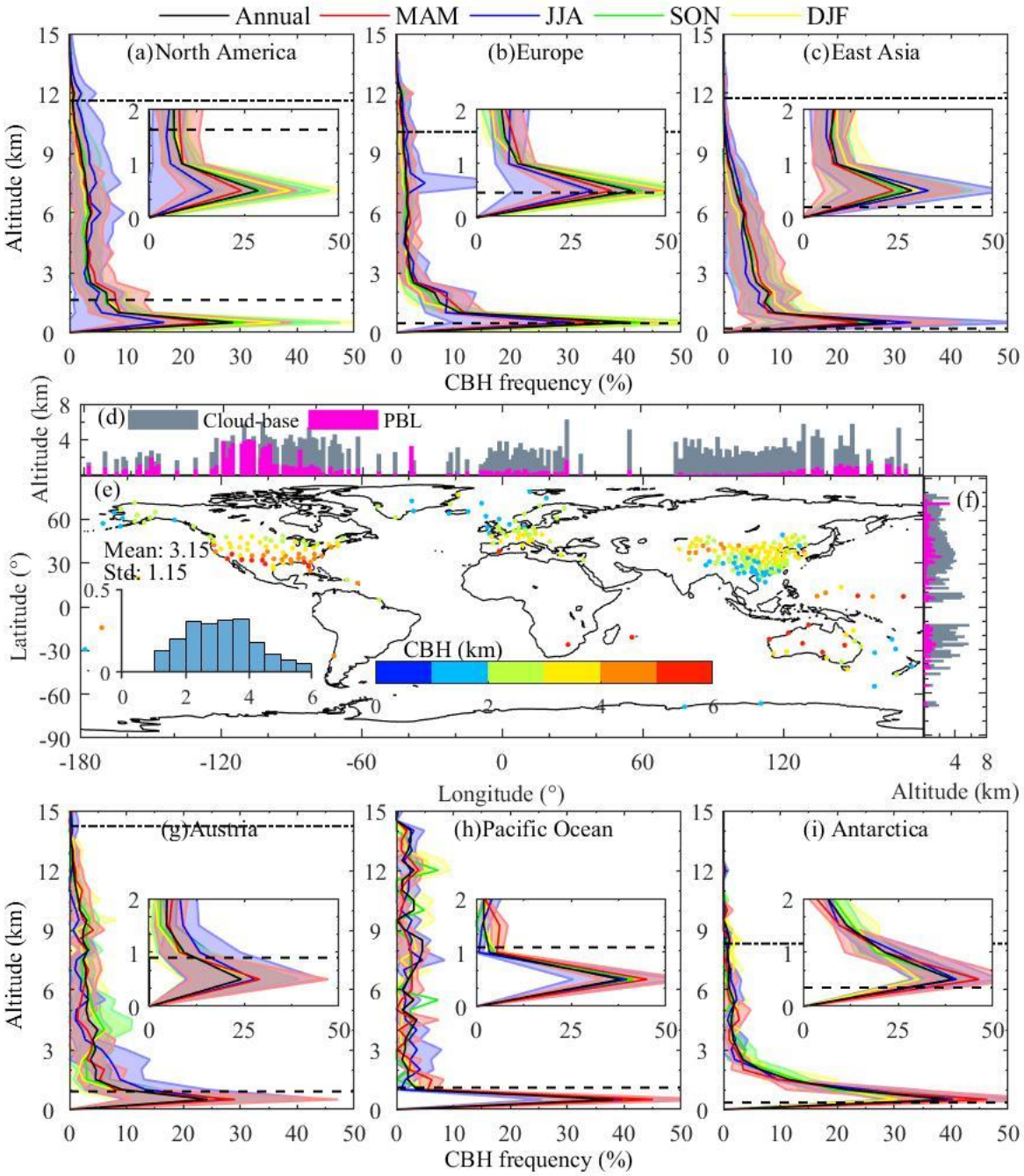

Figure S6. Regional mean vertical distributions of the occurrence frequencies of CBHs at 0000 UTC during the period of 2018–2019. The altitude resolved annual and seasonal averaged occurrence frequencies of CBHs are displayed in (**a**, **b**, **c**, **g**, **h**, and **i**) over six regions of interest, including North America, Europe, East Asia, Austria, Pacific Ocean, Polar. Also shown are the near-global geographic distribution of the annual mean CBH (**e**), with the histogram of the probability distribution for CBH in the inset and the corresponding meridional (**d**) and zonal (**f**) means overlaid with the mean PBLH.

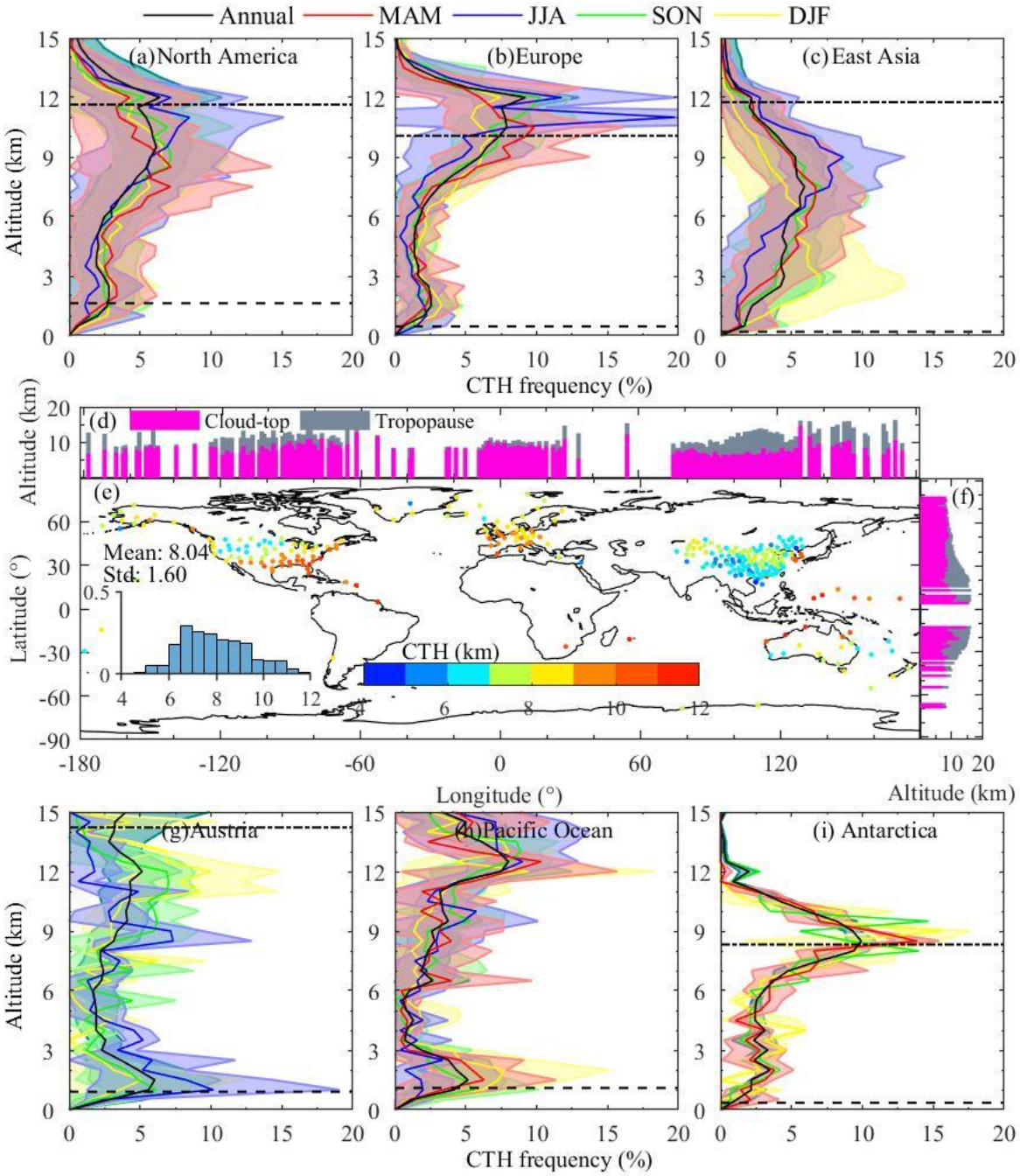

Figure S7. Similar as Fig. 6, but for the occurrence frequencies of CTHs at 0000 UTC during the period of 2018–2019.

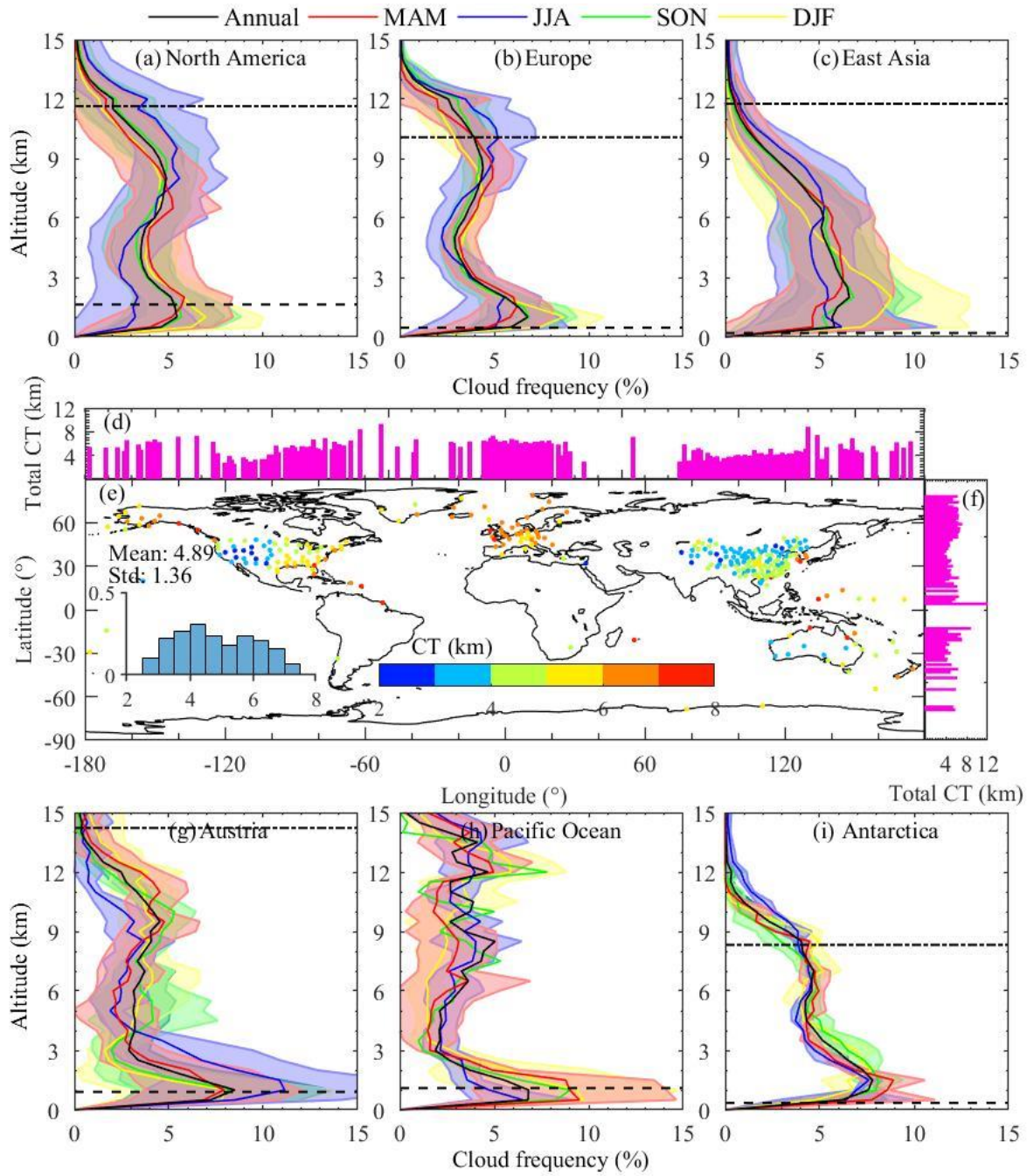

Figure S8. Similar as Fig. S6, but for the occurrence frequencies of clouds at 0000 UTC during the period of 2018–2019.

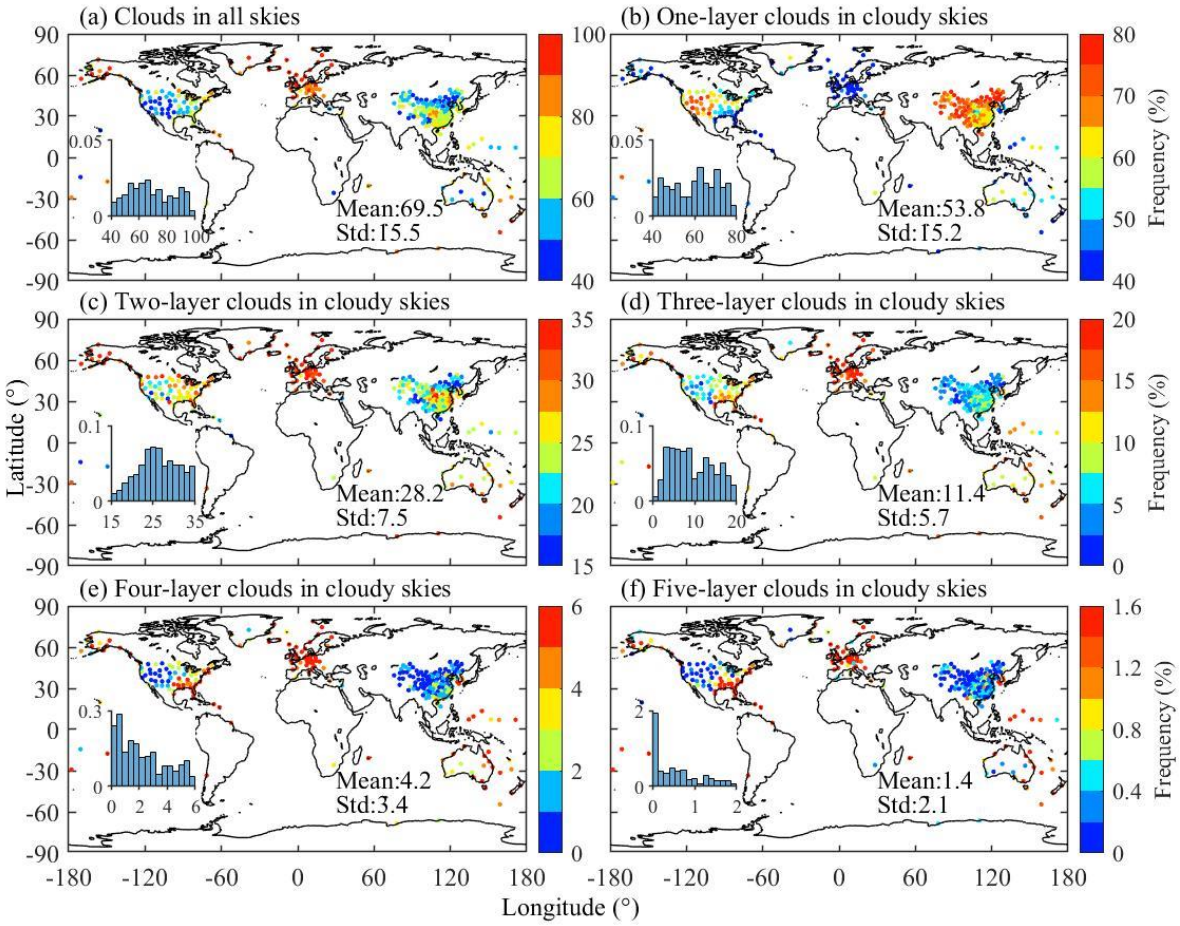

Figure S9. The geographic distributions of the occurrence frequencies of (**a**) clouds in all skies, and (**b**, **c**, **d**, **e**, and **f**) one-, two-, three, four-, and five-layer clouds in cloudy skies at 0000 UTC during the period of 2018–2019. It should be noted that the range of the color bar differ a lot in order to improve the visual interpretation. Also shown are the histograms of probability distributions for the cloud occurrence frequencies in each panel.

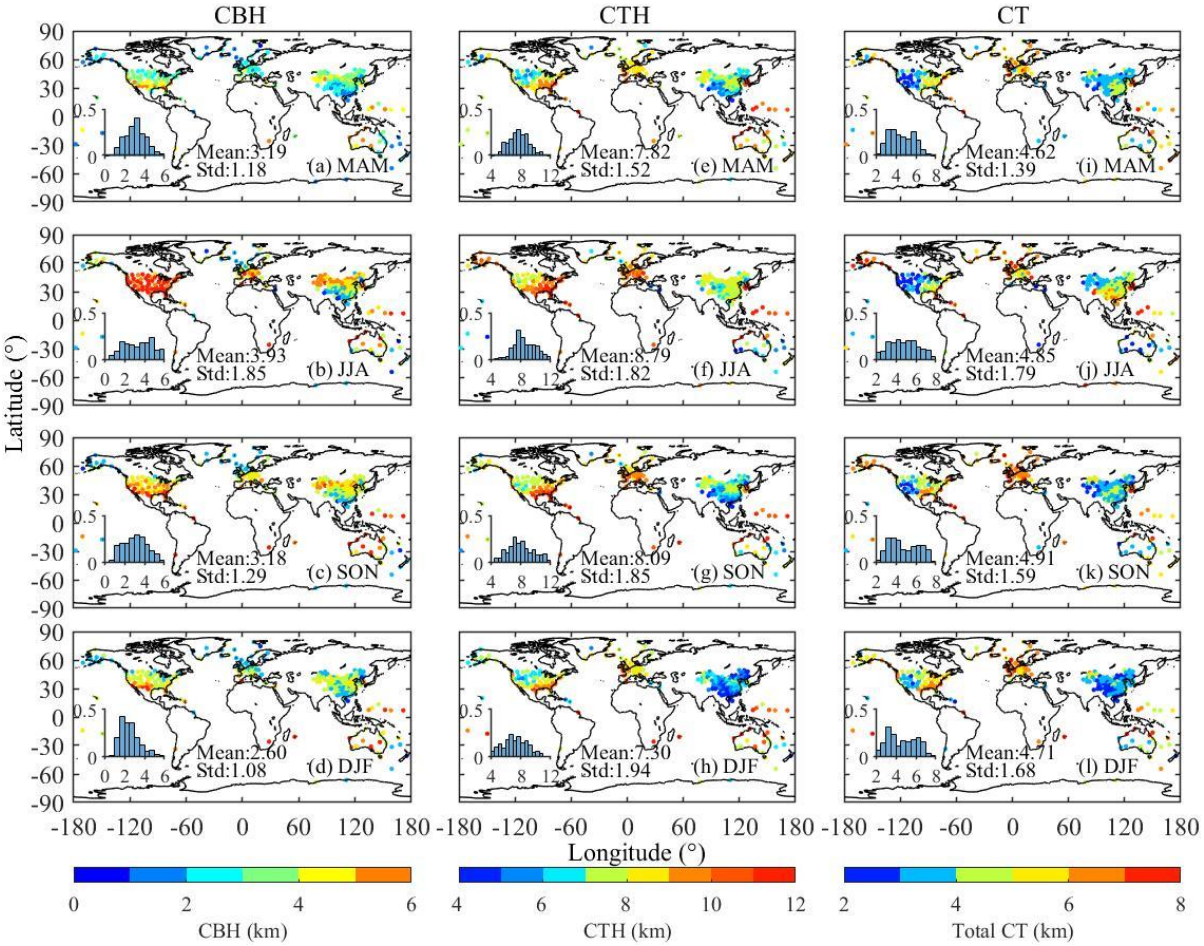

Figure S10. The geographic distributions of the seasonal mean CBHs (**a**, **b**, **c**, and **d**), CTHs (**e**, **f**, **g**, and **h**), and CTs (**i**, **j**, **k**, and **l**) at 0000 UTC during the period of 2018–2019. Also shown are the histograms of probability distributions for the CVS in each panel.

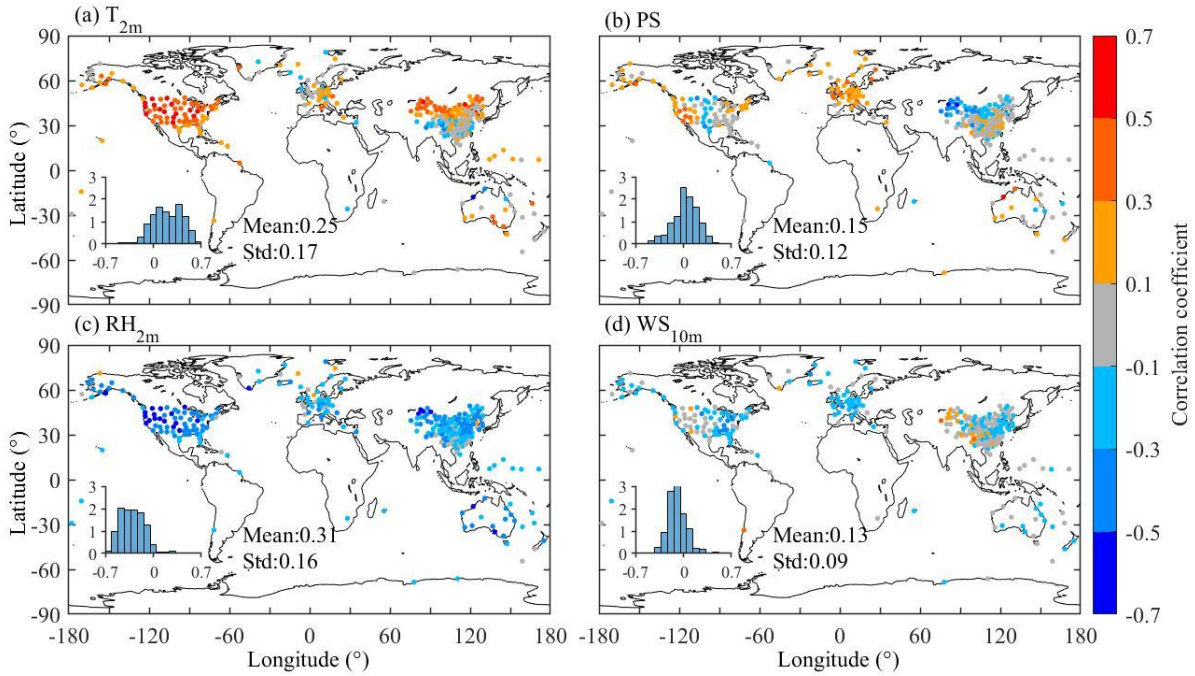

Figure S11. Geographic distributions of the correlation coefficients (R) between radiosonde-derived CBH and surface meteorological variables: (**a**) 2m air temperature (T_{2m}), (**b**) surface pressure (PS), (**c**) 2m relatively humidity (RH_{2m}), and (**d**)10m wind speed (WS_{10m}) at 0000 UTC during the period of 2018–2019. Also shown are the histograms of probability distributions for their corresponding R values in each panel.

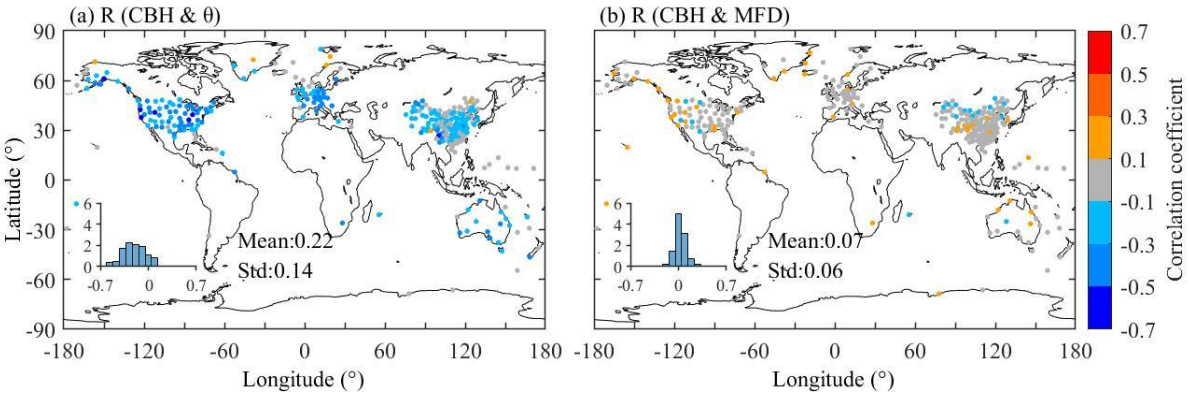

Figure S12. The same as Fig. S11, but for the correlations between CBH and (**a**) soil water content (θ) and (**b**) moist flux divergence (MFD) at 0000 UTC during the period of 2018–2019.

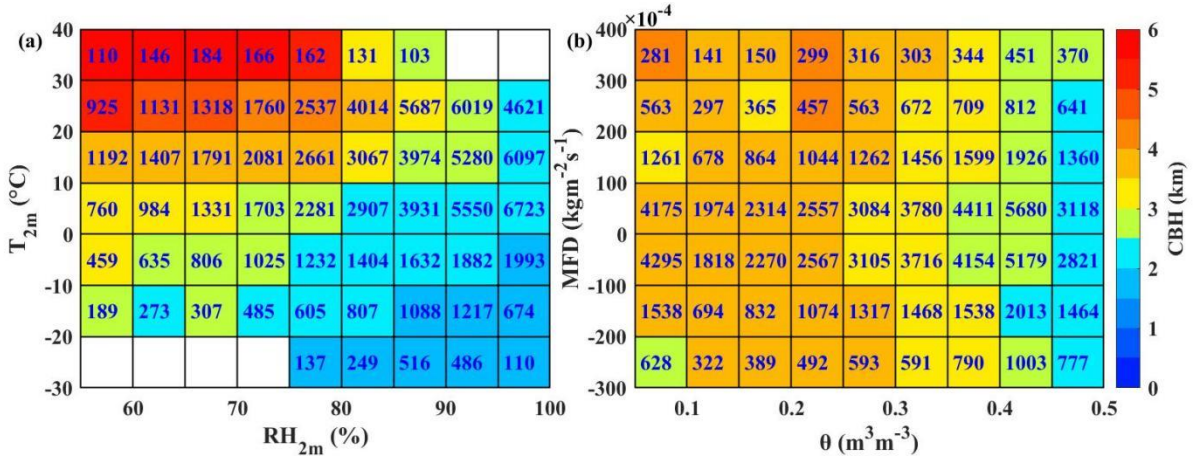

Figure S13. Joint dependences of CBH on (**a**) T_{2m} and RH_{2m}, (**b**) θ and MFD at 0000 UTC during the period of 2018–2019. Note that the number labeled in each cell represents its corresponding sample size.